EXPERIMENTAL STUDY ON AUTOCORRELATED FEMTOSECOND-LASER ABLATION OF MONOLAYER TRANSITION METAL DICHALCOGENIDES

by

Joseph Obeid

A thesis submitted to the faculty of
The University of North Carolina at Charlotte
in partial fulfillment of the requirements
for the degree of Master of Science in
Applied physics

Charlotte

2020

Approved by:

_____
Dr. Tsing-Hua Her

_____
Dr. Yong Zhang

_____
Dr. Haitao Zhang

ABSTRACT

JOSEPH AHMAD OBEID. Experimental study on autocorrelated femtosecond-laser
ablation of transitional metal dichalcogenides. (Under the direction of
DR. TSING-HUA HER)

In this experimental study, we use a pair of 800 nm 180 fs ultrafast laser pulses to
explore time-resolved enhanced ablation of two monolayer transitional metal
dichalcogenides (TMDs). A 2D crystal structure gives monolayer TMDs their unique
properties including a direct electronic band gap, large excitonic resonances, and strong
light-matter interactions. As a result, TMDs are of primary interest in optoelectronics.
Our TMD samples are CVD grown molybdenum disulfide (MoS_2) and tungsten disulfide
(WS_2). For comparison, another common ultra-thin material, graphene, is studied. Our
optical setup provides sub 100 femtosecond resolution by using a variable delay stage
that allows up to ±433 ps delay between pulses. Fundamentally, below some fluence
threshold, the first incident pulse will interact with the sample, producing a memory that
temporarily affects its electronic behavior. If the second pulse arrives before this memory
dissipates, an enhanced ablation process will ensue. To characterize the evolution of this
phenomenon, we analyze the autocorrelated ablation area-delay and ablation threshold-
delay relationships. From our measurements, we extract the lifetimes of the enhanced
ablation processes and draw conclusions on the photoelectronic nature of our TMDs. Our
results show that the enhanced ablation process in MoS_2 has a mean lifetime of ~32 ps
with total enhancement ending after 150 ps. This agrees with the partial mean lifetime of
C-excitons derived in previous pump-probe experiments. Extracted lifetimes for WS_2
demonstrate two possible ablation dynamics. The first lifetime is 58 ps, on par with the

relaxation of the A-exciton after excitation, while the second is a much slower decay process in the ~700 ps regime. Graphene shows evidence for coulomb explosion in the sub ps regime with a secondary peak resonance at ~150 ps and no ablation beyond 250 ps. The ablation threshold for MoS_2 demonstrates a mostly linear dependence on delay while the WS_2 threshold shows two distinct linear regimes. For both, their dependence degrades below ~1ps where bandgap renormalization begins to take place and the carrier dynamics are drastically different from later delays.

ACKNOWLEDGMENTS

Foremost, I would like to thank my thesis advisor and professor, Dr. Tsing Hua-Her for his support, enthusiasm, and patience throughout my master's studies and research. I could not have asked for better guidance from anyone else. The feedback from my other committee members, Dr. Yong Zhang and Dr. HaiTao Zhang, was invaluable and greatly appreciated. Also, I would like to express my sincere gratitude to my lab cohort and PhD student's Joel Solomon and Sabeeh Ahmad for their tireless support and insight on my thesis research, especially with solving numerous problems in the experimental setup. Finally, I would be remiss if I did not thank my parents, Jodi and Nick Obeid, for their undying support throughout my academic career and raising me to be the man I am today.

TABLE OF CONTENTS

LIST OF FIGURES

LIST OF ABBREVIATIONS

TMD	Transition metal dichalcogenide
MoS_2	Molybdenum disulfide
$MoSe_2$	Molybdenum diselenide
WS_2	Tungsten disulfide
WSe_2	Tungsten diselenide
$MoTe_2$	Molybdenum ditelluride
CVD	Chemical vapour deposition
MoO_3	Molybdenum trioxide
Al_2O_3	Aluminum oxide (sapphire)
PL	Photoluminescence
AFM	Atomic force microscope
CW	Continuous-wave
CRT	Cathode-ray tube
BBO	Beta Barium Borate
SHG	Second-harmonic generation

CHAPTER 1: INTRODUCTION

The primary purpose of this study is to characterize the enhanced ablation process of two common monolayer Transition Metal Dichalcogenides (TMDs). They are molybdenum disulfide (MoS_2) and tungsten disulfide (WS_2). Both of these ultra-thin semiconductors have shown promising results in numerous optoelectronic applications. For comparison, another semiconductor-like 2D material, graphene, will also be studied. This is accomplished by two-pulse autocorrelated laser ablation. Firstly, the three major components involved in the study will be introduced. They are femtosecond-laser ablation, monolayer TMDs, and two-pulse autocorrelation. Next, the experimental set-up will be exhibited as well as the accompanying experimental procedure. The results will be presented for the two types of experiments conducted and then discussed. Finally, all of the findings will be summarized.

1.1 Ultrafast Pulsed-Laser Ablation

Laser ablation is the well-established practice of removing material from a solid or liquid substrate via irradiation by a laser source. Typically, low incident laser power heats the target substrate, causing evaporation or sublimation. When at high power, the laser can directly convert the target material to plasma. This quick and effective breakdown of material has many applications in nanotechnology fabrication, micro packaging, deposition of thin dielectric and metallic films, and even surgery.

Continuous-wave (CW) laser ablation can induce complicated chemical reactions from heating and excitations in a material, changing its fundamental properties. With the development of the ultrafast laser came femtosecond pulsed lasing where the optical

power appears in pulses with a short duration ($\sim 10^{-15} s$). The energy contained in each

optical pulse E_p is given in equation 1.1.

$$E_p = \frac{P_{ave}}{RR} = P_{ave} * T \tag{1.1}$$

The average power P_{ave} of the pulse can be measured by averaging the energy

over some time interval. In this case, the time interval is the period T of a pulse in the

pulse train. The pulse repetition rate RR is the number of emitted pulses per a second or

the pulse frequency.

The peak power P_{peak} of a pulse differs from P_{ave} in that it depends on the pulse's

temporal shape. It represents the maximum power of any point of time for the duration of

the pulse. Equation 1.2-4 shows P_{peak} for three common pulse temporal shapes: Square,

Gaussian, and Sech^2.

$$Square: P_{peak} = \frac{E_p}{\Delta\tau} = P_{ave} * \frac{T}{\Delta\tau} \tag{1.2}$$

$$Gaussian: P_{peak} \approx 0.94 \frac{E_p}{\Delta\tau} \approx 0.94\, P_{ave} * \frac{T}{\Delta\tau} \tag{1.3}$$

$$Sech^2: P_{peak} \approx 0.88 \frac{E_p}{\Delta\tau} \approx 0.88 P_{ave} * \frac{T}{\Delta\tau} \tag{1.4}$$

$\Delta\tau = \tau_{FWHM}$ represents the length of the pulse in time or the Full Width Half

Maximum (FWHM) of the intensity as a function of time. Given that the distance from

the center of the beam to where the intensity falls off by $1/e^2$ is the gaussian beam radius

w_0, the peak intensity I_{peak} is then

$$I_{peak} = \frac{P_{peak}}{(\pi w_0^2 / 2)} \tag{1.5}$$

1.5 represents at least one cycle averaged Poynting vector. It is the intensity at the peak of the pulse envelope and is also cycle averaged.

The peak fluence is the energy per a unit area at the highest point of the spatial profile. It has no dependence on the pulse duration and is shown in equation 1.6.

$$F_{\text{lu}} = \frac{E_{\text{p}}}{(\pi w_0^2/2)} \tag{1.6}$$

Finally, using Liu's technique for measuring pulsed Gaussian-beam spot sizes[1], the area of an ablation crater can be fit to equation 1.7.

$$\text{Ablation area} = \frac{\pi w_0^2}{2} \ln\left(\frac{F_{\text{lu}}}{F_{th}}\right) \tag{1.7}$$

F_{th} is the ablation threshold in terms of fluence. It is the minimum fluence required to cause any measurable ablation.

Femtosecond laser ablation allows the process and evolution of ablation to take place almost instantaneously with each incident pulse. This reduces the problem of shielding from the latter parts of the pulse by an ablation plume[2]. Any craters or plasmas produced on a target sample from such laser ablation will heavily depend on the characteristics of the surrounding environment, the nature of the substrate, and the laser itself including wavelength of light, pulse duration, pulse repetition rate, and pulse energy.

Figure 1.1: Periodic table with highlighted TMD elements

1.2 Transition Metal Dichalcogenide Monolayers

Transition Metal Dichalcogenide (TMDs) are chemically of the form MX_2 with M being a transition metal atom in groups 4-10 of the periodic table and X being a chalcogen atom in group 16. In typical bulk form, they have three polytypes or stacking structures[3] including hexagonal (2H), rhombohedral (3R), and trigonal (1T) where each individual layer is generally around 6.5 Å. Consequently, bulk TMDs exhibit diverse properties acting as an insulators, semiconductors, or even true metals. Many of the physical properties of these highly anisotropic crystals have been studied extensively, but there is still much to learn.

Interestingly, semiconductor TMDs have a shift in their electronic band structure from an indirect to a direct bandgap as they are reduced from a bulk form to fewer and fewer layers. TMD monolayers are atomically thin (one layer thick) and are often classified as two-dimensional materials. Their 2D structure results in strong quantum confinement and high dielectric screening which produce large exciton binding energies and strong excitonic resonances[4]. As direct bandgap semiconductors, they have stable

excitons at room temperature and produce strong light/matter interactions. Molybdenum disulfide (MoS2) is a well-studied TMD whose band gap energy increases from 1.2 eV to 1.8 eV at the monolayer limit[5]. Some other common TMDs used in electronics as transistors, and optics as detectors or emitters are WS2, MoSe2, WSe2, and MoTe2.
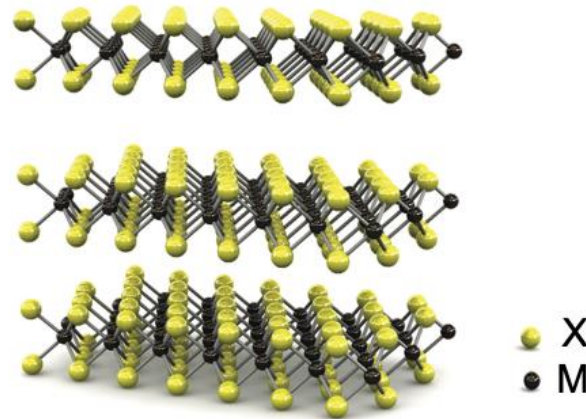
Figure 1.2: Atomic illustration of TMDs in the chemical form XM_2

Graphene is a single layer of carbon atoms and a popular alternative 2D semi-conductor-like material with no electronic bandgap. A TMD like MoS_2 has a high charge carrier mobility similar to that of graphene making them both useful when incorporated into transistors. However, MoS2 also demonstrates a low threshold voltage and high ON/OFF current ratio ($\sim 10^8$)[6]. Another advantage of monolayer TMDs comes from their mechanical stability. MoS_2 has a Young's Modulus (E_{Young}) of 270 GPa[7] which is greater than that of stainless steel, and it has a high strain limit ($\sim 10\%$ E_{Young}). Such stability allows for strong reversible excitation that is not possible in bulk form. Moreover, MoS2 will retain its crystal structure at a fluence of 70% of the ablation threshold whereas bulk

materials will undergo amorphization. Finally, at the monolayer limit, TMD's exhibit highly nonlinear optical behavior including high harmonic generation[8].

<div align="center">1.3 TMD Fabrication</div>

TMDs are typically fabricated via mechanical exfoliation or chemical vapour deposition (CVD). The former of which can be accomplished due to the relatively weak Van-der-Waals forces holding the crystal layers together. A solid micro-cleaver easily separates crystal layers without breaking the chemically bonded transition metal and chalcogen atoms. Typically, this is accomplished by abrading bulk TMD with another solid to produce monolayer flakes with a size of 5-10 microns that are then deposited onto a substrate[9].
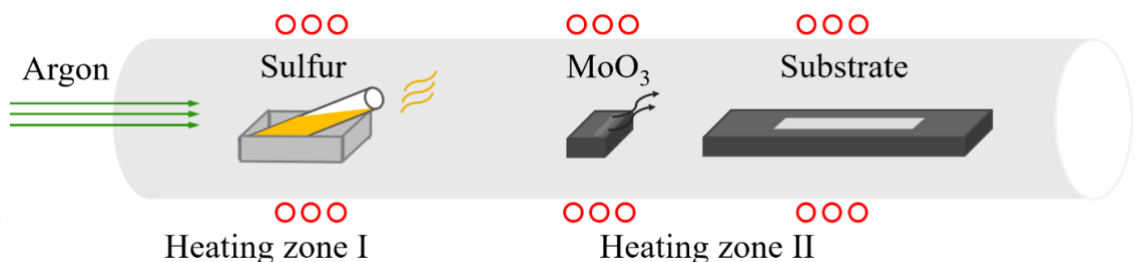
Figure 1.3: Fabrication of MoS_2 via the CVD process

CVD is the more versatile process of growing the TMD on a substrate by having volatilized TMD precursors heated and exposed to gases that can catalyze the formation of the crystal. In general, CVD produces larger flakes/films with a size of 5-100 microns in diameter of the desired TMD[10], making the samples an easier target for ablation.For this reason, the samples used in this study were CVD grown. Figure 1.3 is a diagram

showing the general fabrication process of MoS2. In an oven, under an Argon flow, gaseous Sulfur and MoO3 react on a sapphire (Al$_2$O$_3$) substrate forming MoS2.

Figure 1.4: Optical microscope images of MoS$_2$, WS$_2$, and MoSe$_2$ sample flakes

Figure 1.4 displays different sample TMD flakes grown on sapphire substrates via CVD. Additionally, an example of MoS$_2$ on sapphire is shown in figure 1.5 where the points A, B, and C correspond the optical images below showing the differe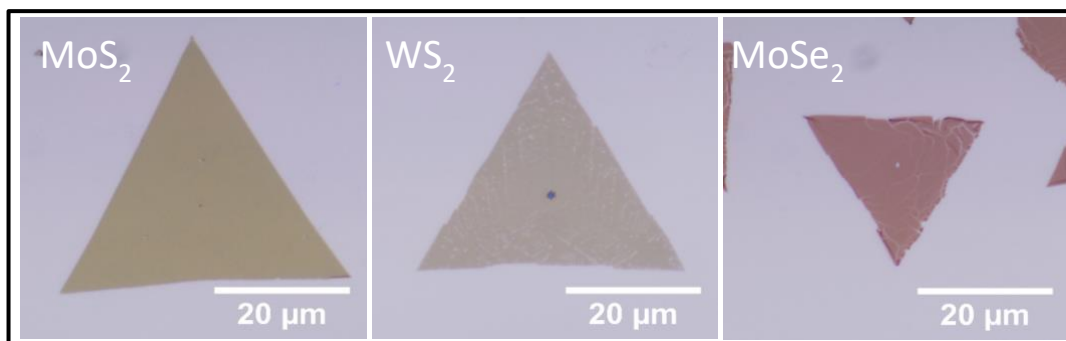nt densities of MoS$_2$ from a continuous film to individual flakes. To ensure monolayer growth, all TMDs are characterized by Photoluminescence (PL), Raman Spectroscopy, and Atomic Force Microscope (AFM) measurements.

When TMDs are ablated, holes/craters are left on the TMD samples where the ablated material was originally located. An example of this is shown in figure 1.6 where a MoS$_2$ sample was ablated three times for each flake. The dark spots are the location where crystallization started during growth. Any other imperfections are due to contaminants or damage during transportation of the sample. The elliptical ablation craters are due to the elliptical mode of the laser. If a laser pulse has too much energy, the impact can penetrate deeper than the TMD sample, damaging the substrate itself.
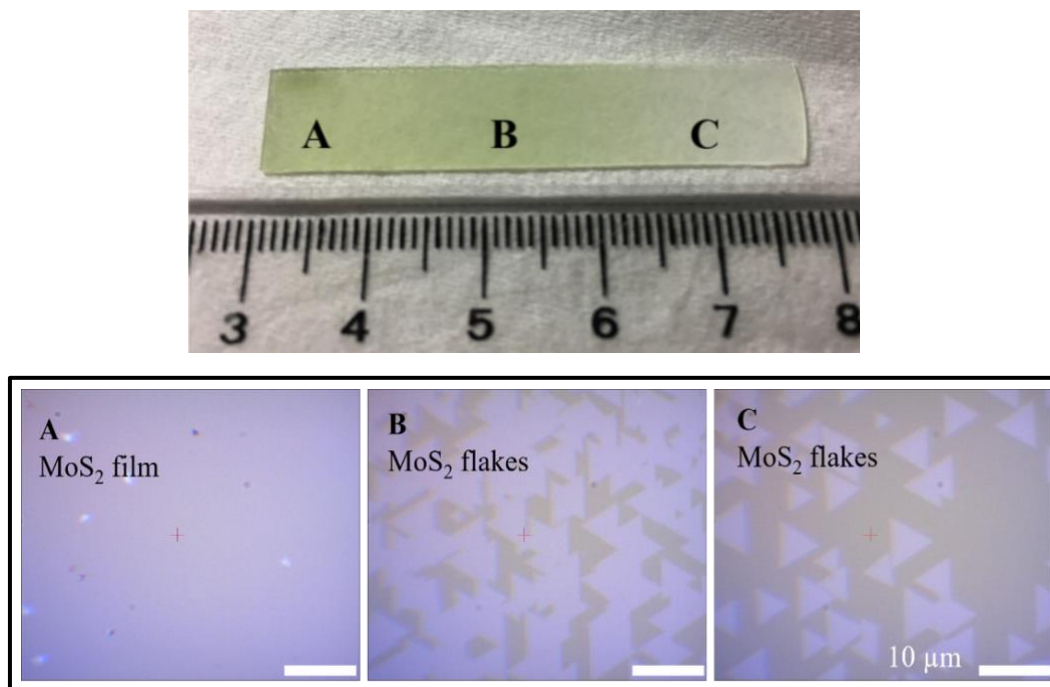
Figure 1.5: CVD grown MoS$_2$ on sapphire substrate with varying continuity

Figure 1.6: Ablated MoS$_2$ flakes on sapphire

1.4 Two-Pulse Autocorrelation

Autocorrelation is primarily a statistical tool yielding the correlation of a signal with a duplicate of itself after some delay as a function of that delay. With pulse lasers, a pulse can be can split into two identical pulses that can be correlated after some time delay of one of the pulses. This autocorrelation of the duplicated pulses and other similar pump-probe methods where both pulses vary in wavelength are invaluable in characterizing the pulse ablation process and its subsequent evolution. This can be accomplished because below some defect energy threshold, when the first pulse strikes a semiconductor material, it produces a temporary electronic memory in that material like exciting charge carriers. And if the second pulse is absorbed before this memory is gone, there is enhanced ablation due to its highly nonlinear behavior. If the two pulses are below the defect energy threshold, when fired separately (at long delays), no ablation or defect will be produced. Two-pulse autocorrelation can then reveal the timescales of the mechanisms that lead to the enhanced ablation.
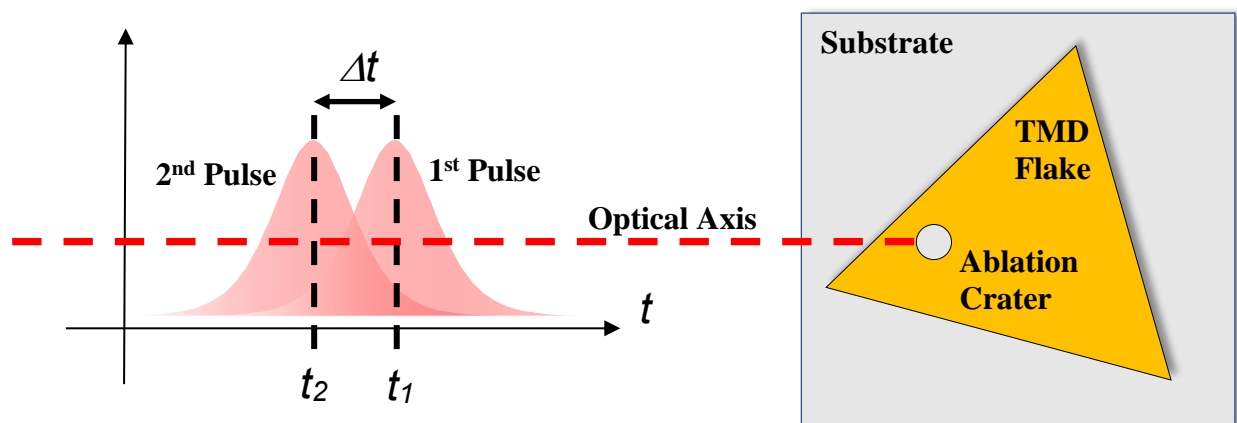

Figure 1.7: Two-pulse ablation of a TMD sample

Since enhanced ablation can take place on the scale of femtoseconds, the autocorrelation will be represented by the ablated crater area as a function of the delay time between the two incident pulses. The area of an ablation crater can be related to the fluence (energy/area) of a pulse as shown in equation 1.7. An illustration for the two-pulse autocorrelation process can be seen in figure 1.7. The 1st pulse arrives at time t_1 and the second pulse arrives at t_2 yielding a delay of Δt.

The ablation area vs delay can be fitted with a standard exponential function as seen in equation 1.8.

$$N(\Delta t) = N_0 e^{\frac{-\Delta t}{\tau}} \tag{1.8}$$

N_0 is the amplitude of the exponential function, τ is the decay constant, and Δt is the pulse delay time. τ is also known as the mean lifetime and can be thought of as a scaling factor that is equivalent to the time it takes for the ablation area to reduce to $\frac{1}{e}$ times its original value. The ablation area vs delay relation may involve multiple exponential terms due to varying decay rates for different delay regimes.

In addition, the ablation threshold F_{th} vs delay relationship will be studied. At a single delay, several two-pulse shots can be fired with varying fluences. A simple logarithmic or power function can be fitted to the ablation areas as a function of fluence as shown in equations 1.9 and 2.0.

$$Ablation\ Area\ = m \log(F_{lu}) + b \tag{1.9}$$

$$Ablation\ Area\ = m(F_{lu})^p + b \tag{2.0}$$

A plot of fluence vs ablation areas is also referred to as a Liu plot[1]. The fluence threshold F_{th} can then be approximated by the x-intercept. This can be done for multiple delays and a line can be fit to the extracted fluence threshold data.

CHAPTER 2: EXPERIMENTAL SET-UP AND METHODS

2.1 Optical Set-up

The laser source was comprised of two Ti:Sappphire oscillators, the Tsunami

mode-locking oscillator and the RegA 9000 regenerative amplifier. Both were situated at

the end of a pneumatically dampened optical table. Firstly, the Millennia CW laser

optically pumps the Tsunami, producing a 80 MHz pulse train at 800 nm with pulse

energies of about 9-10 nJ. The RegA is pumped via the Verdi V18 CW laser and seeded

by the output beam of the Tsunami. At which point the RegA uses Q-switching to select

out pulses and energize those chosen. The final output beam had a pulse repetition rate of

100 kHz at 3 μJ per a pulse. The laser system is pictured in figure 2.1 and overlayed with
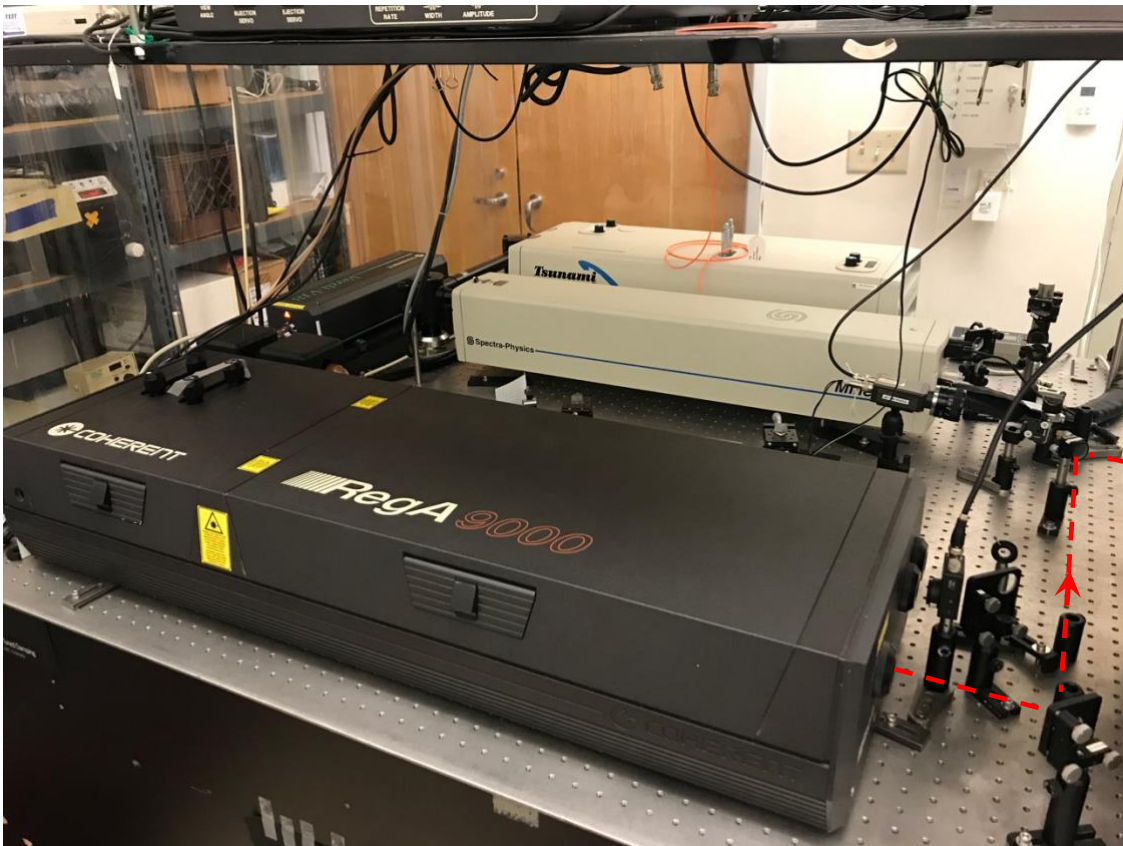
the optical path of the output beam.
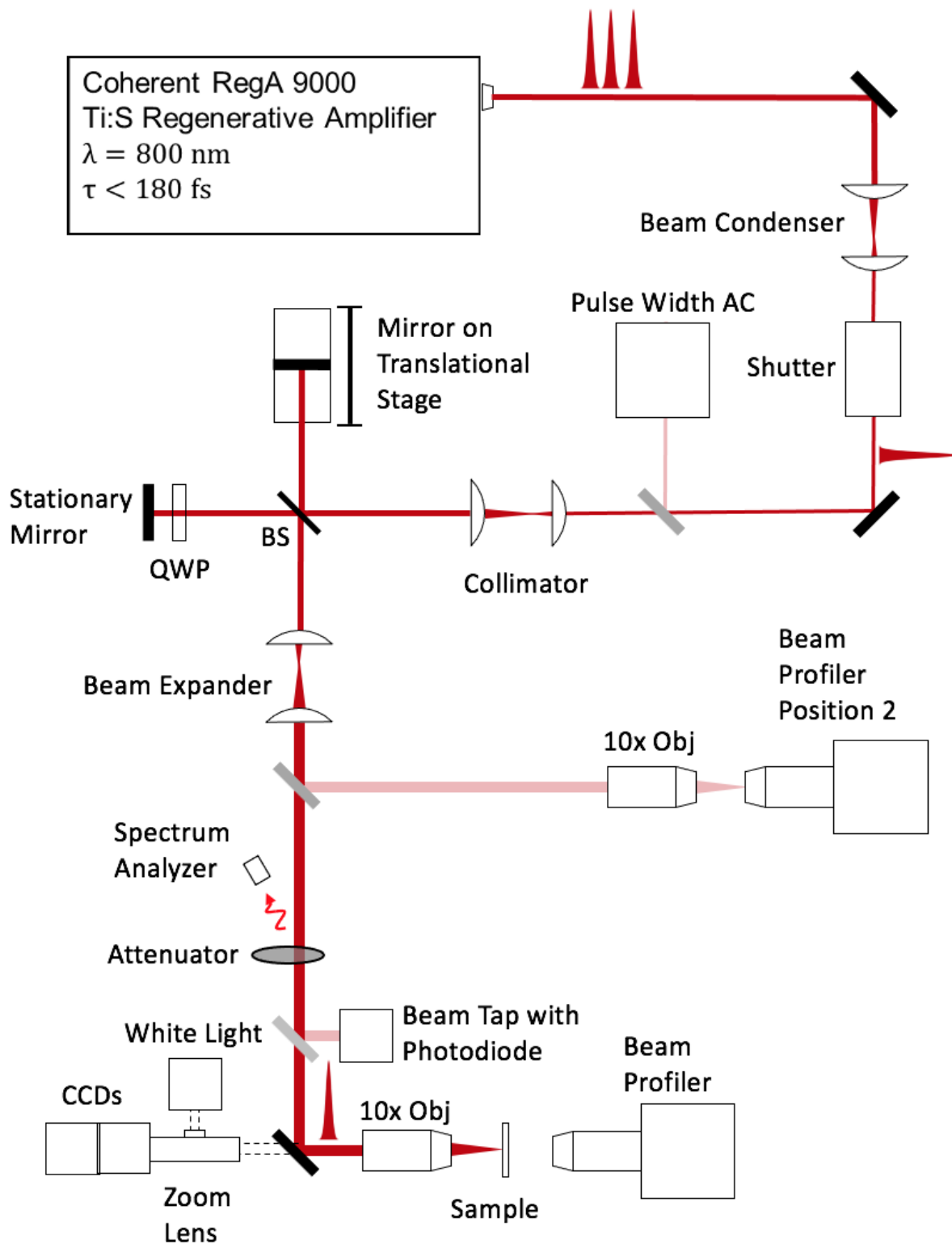

Figure 2.1: Pulsed-laser system

Figure 2.2: Schematic of experimental set-up

A labelled schematic of the entire experimental set-up is given in figure 2.2. The depicted beam path is simplified compared to the actual experimental set-up to aid in clarity. Moreover, some of the trivial optical components are not included. All of the experiments were conducted a few meters away from the laser source. The following figures are images of various parts of the physical set-up. In order to fit the beam through a shutter aperture (2), a simple two-lens refracting telescope (1) condenses beam. Before any experimentation, the shutter is left open allowing the entire RegA beam and pulse train to propagate through the set-up for alignment and diagnostic purposes. A flipper mirror was deployed to redirect the beam into a separate home-built collinear autocorrelator (3) used to measure pulse width. This first autocorrelator is in the form of a Michelson interferometer that uses a type-I Beta Barium Borate (BBO) crystal to induce nonlinear second harmonic generation (SHG). The output 400 nm light is sent into a photodiode that measures its intensity amplitude fluctuations.
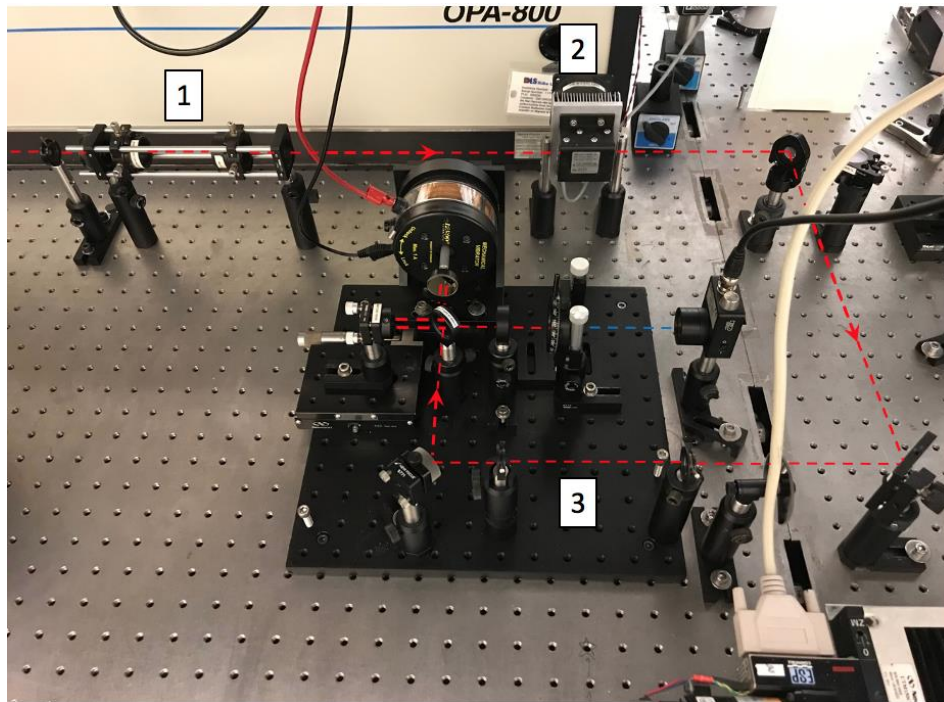

Figure 2.3: First section of the optical set-up

When the pulse-width autocorrelator is not in use, the beam is directed through another collimating two-lens telescope (4) that corrects for diffraction arising from the long distance that the beam propagates. Then, the beam enters a second collinear autocorrelator that also takes the form of a Michelson Interferometer and is used during experiments. A thin beam-splitter (5) splits the incoming beam into two, with one reflecting down a translation arm (6) and the other transmitted down a stationary arm (7). The stationary arm has one retroreflecting mirror fixed in place approximately 18 cm from the beam-splitter. The translation arm has a similar retroreflecting mirror fixed to linear motorized stage at approximately the same distance. The stage can translate the mirror about 65 mm along the optical axis in both the forward and backward directions. Resultantly, a pulse travelling on the translation arm can be time delayed with respect to the pulse on the stationary arm by up to 433 ps in either direction.

The base of the stage is an aluminum block that spans its length and was specially machined for this application. The stage is clamped down using the bored screw holes lining the sides of the block. The thick aluminum isolates the stage from vibrations, relieves mechanical strain on the stage bearings, and reduces mirror tilt during translation. Consequently, the beam drift that can occur when the mirror is translated long distances is kept at a minimum.

In order to prevent interference between the two output beams, their polarizations are set orthogonal to each other by inserting a quarter-wave plate along the stationary arm. Thus, the stationary arm is horizontally polarized (s-polarized) while the translation arm is vertically polarized (p-polarized). Once exiting the autocorrelator, the newly

recombined beam is immediately expanded with yet another refracting telescope (8) so that the beam spot completely fills the aperture of the sample objective.
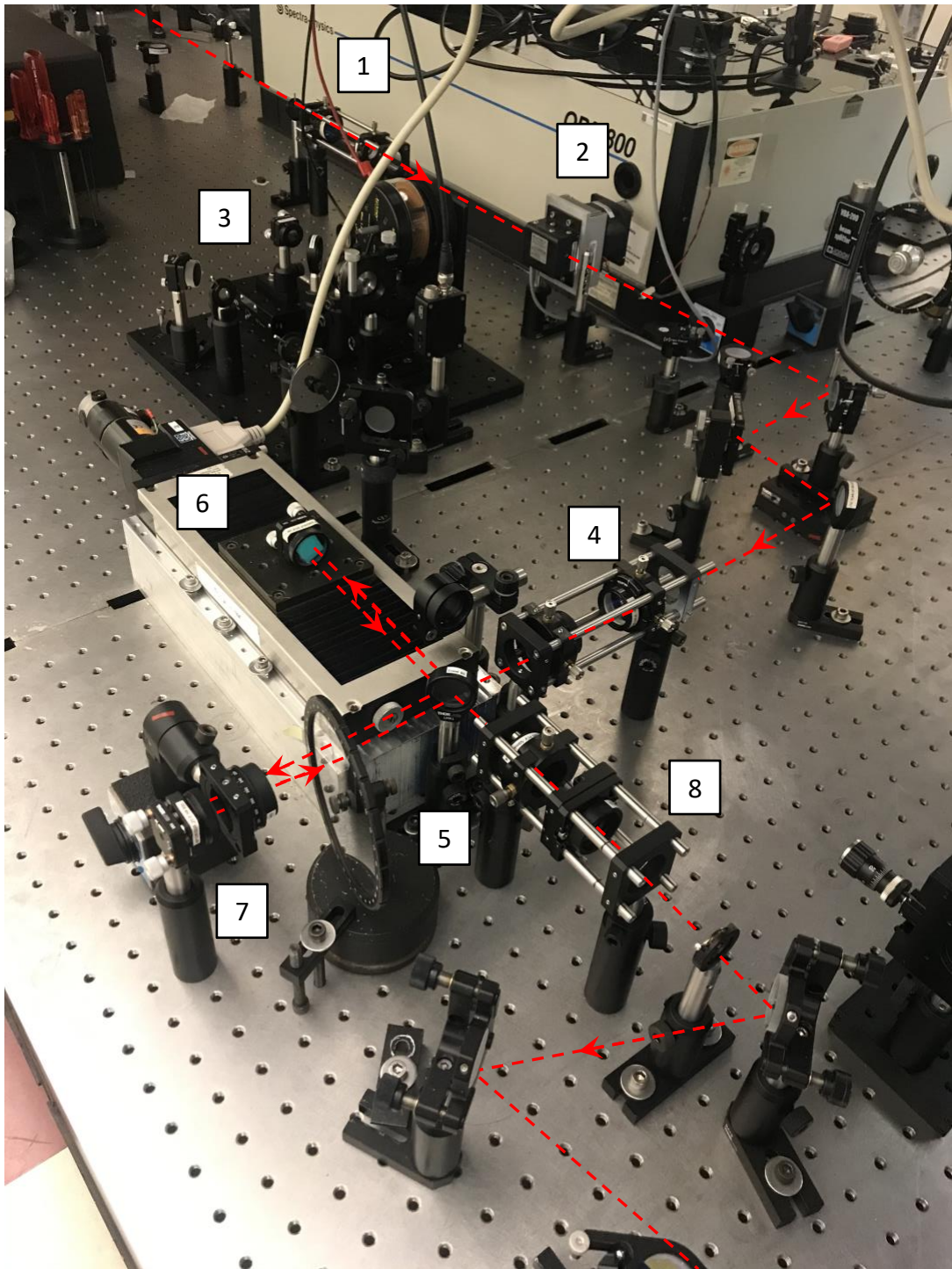
Figure 2.4: Primary collinear autocorrelator

Before reaching the objective, the beam is partially transmitted through a backside polished mirror. It travels across the optical bench and is focused down via a 10X objective into a home-built microscope (9) coupled to a pixel-array camera. The camera is digitally connected to a computer with DataRay software used to measure the beam spot profile. The large separation distance between the primary autocorrelator and beam profiler allows for higher resolution when overlapping the two arms.
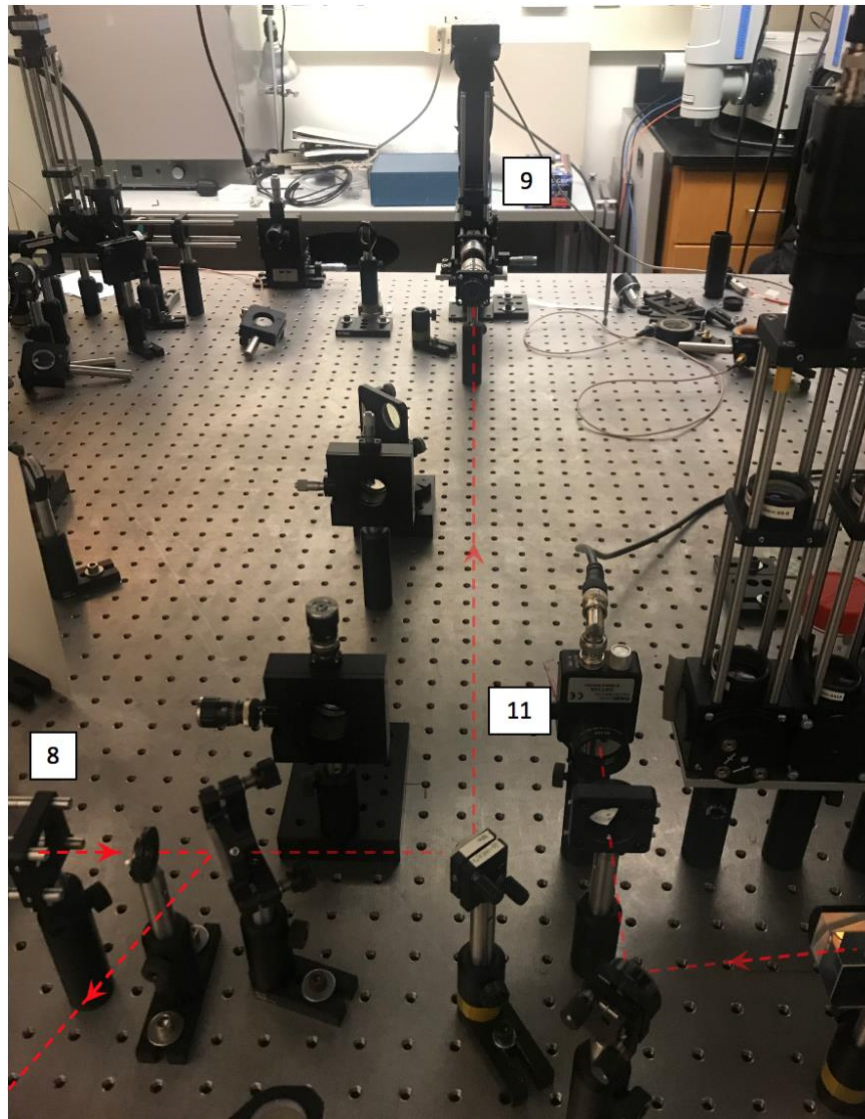
Figure 2.5: Beam profiler in 2nd position

The major portion of the beam that reflects off the backside polished mirror soon passes by a Avantes Spectrometer (10) coupled to a ground-glass sensor that is used to measure the beam spectrum. Soon after, the beam is attenuated by passing through a variable neutral density (ND) filter. A tap reflects a small portion of the beam intensity into a photodiode (11) that measures the amplitudes of the pulses in the pulse train. The photodiode shows some polarization bias. Therefore, a polarized beam splitter is introduced before the diode to block the translation arm's contribution so that only amplitudes from the s-polarized stationary arm are measured.
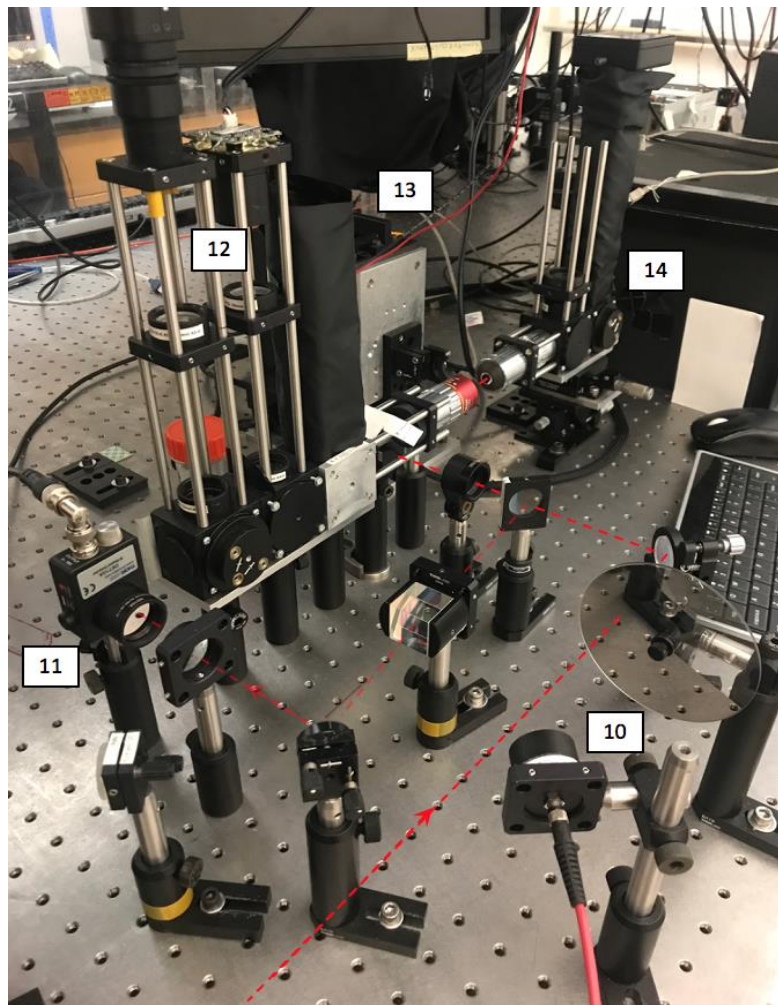
Figure 2.6: Final section of the optical set-up

Finally, the beam reaches the sample objective that is coupled to another home-built optical microscope (12). The objective is a Mitutoyo M Plan Apo NIR objective (10X/ 0.26, ∞/0 f=200) that focuses the laser beam onto the sample. The sample microscope has three optical paths as illustrated in figure 2.7 with two cameras that are each connected to their own analog CRT screen. The light-source path houses a white-light LED that is used to illuminate the sample. One of the imaging optical paths was optimized to detect the white light back-reflection from the sample, yielding a relatively well resolved image of the sample on one of the CRT screens. As a result, the location of the of the beam on the sample can be monitored. The second imaging path was filtered to detect 800nm light, allowing it to display the back-reflected image of the beam spot on the other CRT screen. With a dedicated beam spot screen, the focus of the beam could be kept in check during experiments.
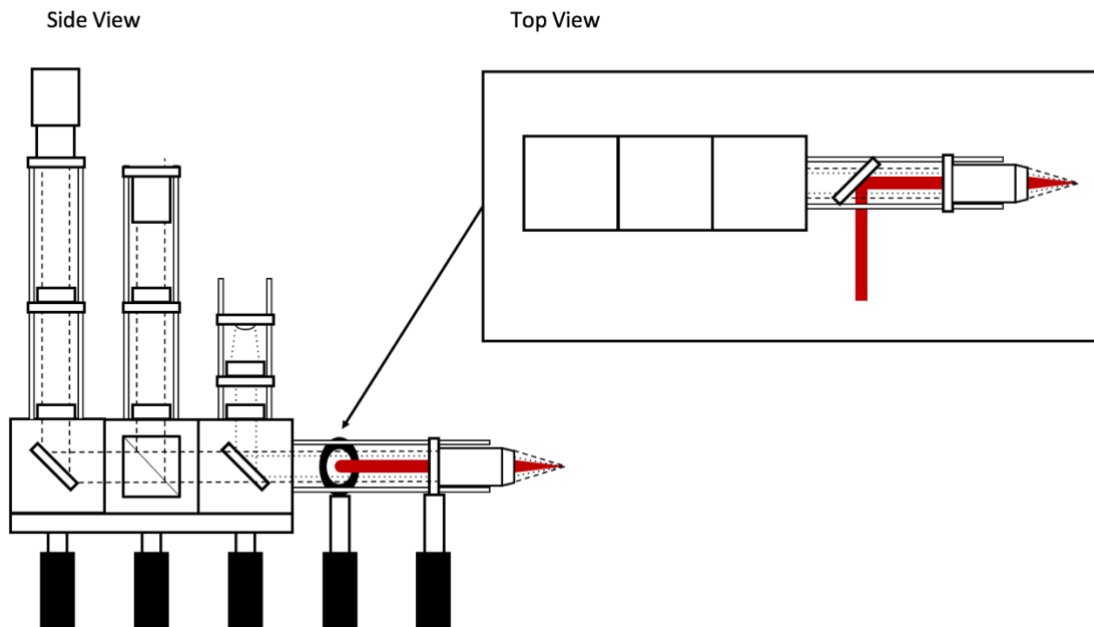
Figure 2.7: Sample optical microscope

The sample is mounted to a Aerotech ANT-50L linear motorized stage (13) that can be translated in all three dimensions when controlled via Aerotech software. The focus of the objective was determined by single shot ablation where a sample was scanned along the optical axis through the beam waist until the largest ablation hole formed corresponding to the highest fluence and thus focus.
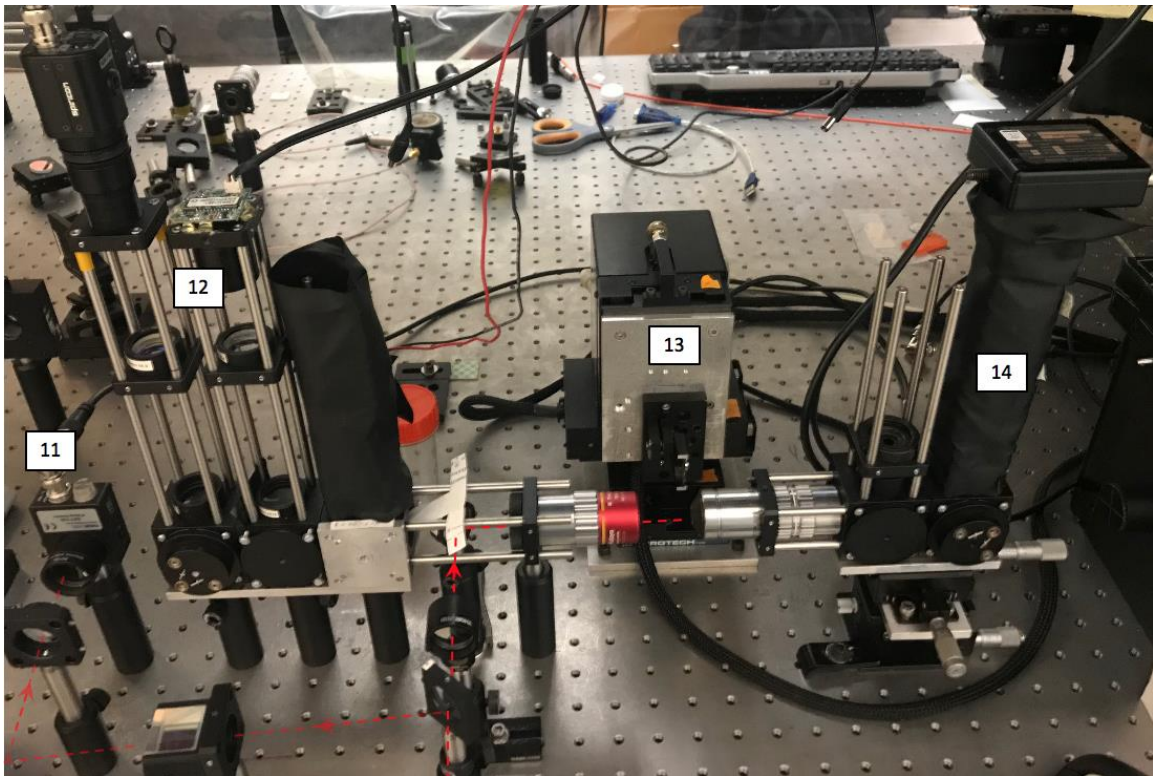
Figure 2.8: Sample section of the set-up

Past the far side of the sample stage is the first location of the beam profiler (14). In this position, the profiler is strictly used to measure the actual beam spot size at focus as well as ensure that the translation and stationary arms are initially overlapped. The sample can be translated out of the way so that the beam profiler can be calibrated using a Air Force target with known dimensions.

2.2 Initial Diagnostics and Procedures

Before experimentation, initial diagnostics of the laser beam are taken. The shutter is opened allowing the entire RegA beam to propagate through the optical set-up. Firstly, the pulse width is measured using the pulse width autocorrelator. A function generator is connected to a PASCO Scientific speaker and is set to 4 Hz. The speaker oscillates one of the mirrors producing an intensity autocorrelation signal on a digital oscilloscope that is saved for post-trial processing.

A paper notecard is placed in front of the spectrum analyzer to intercept the beam. The back scattered 800 nm light is detected by the ground glass sensor. Avantes spectrographic software displays then records the spectrum of the RegA beam. The spectrum FWHM is kept around 10.5 nm before the sample objective and can be tuned by closing down a pinhole aperture near the RegA. The output pulse energies for both AC arms are measured with a photodiode and set equal by adjusting a variable ND filter along the stationary arm.

Next, the beam profiler is fixed into its first position and translated so that the beam spot is in focus and imaged on the DataRay software. Both arms of the autocorrelator are overlapped by adjusting the stationary mirror only. The translation mirror is not adjusted since alignment is sensitive to stage translation. The beam profiles are measured for the stationary, translation, and both overlapped arms.

A LabVIEW program was designed to allow for mirror translation to any input position on the translation stage. No time delay between the two arms is found by moving the translation mirror to approximately the same distance from the beam splitter as the stationary mirror (18 cm). A polarizer is set to 45° and placed before the objective

to match the polarizations of both arms. Then, a type I BBO crystal is moved into the objective focus and tuned to maximize phase matching. A lens focuses the generated second harmonic (400 nm) into a photodiode where interference fringes are measured as amplitude fluctuations on an oscilloscope. The translation stage is scanned in one direction until the maximum amplitude is found, corresponding to time-zero.

2.3 Trial Procedures

The RegA's pulse repetition rate is tuned to 615 Hz during experiments. First, the sample is aligned into focus with the sample stage. Using the Aerotech software, a section clear of contaminants or defects is found on the sample. This area of the sample is mapped out by hand on paper so that the ablated regions can be found on an optical microscope after the trial. Throughout a trial, another LabVIEW program is used in conjunction with a digital oscilloscope connected to the pulse amplitude photodiode to control the shutter and measure each pulse shot. The program commands the shutter to select one pulse from the RegA pulse train. The shutter is opened periodically during a trial to check the amplitude fluctuations from the RegA and improve the AC beam spot overlap.

Next, one arm of the autocorrelator is blocked and two shots are fired individually spaced by a few seconds. This simulates a delay between two pulses at the limit of infinity and ensures no actual enhancement can take place. The variable ND filter is adjusted to attenuate the pulse amplitudes and two-shots are fired multiple times at different locations on the sample until no ablation occurs. All of the trials are conducted below this two-shot threshold energy. Finally, both arms are unblocked, and the trial can begin.

For trials studying the ablation area-delay relationship, only one pulse energy below a two-shot threshold is used. The sample is ablated at various delays from 0 ps to 433 ps for a minimum of five single shots per a delay. Each shot amplitude is measured and recorded on the LabVIEW program. Trials studying the ablation threshold-delay relationship uses five different pulse energies below a two-shot threshold per a delay. Five shots are done for each pulse energy resulting in 25 total shots per a delay.

As with before the trial, the pulse width, spectrum, and beam profiles are all recorded again to ensure that the laser properties did not deviate enough to affect the ablation process throughout the trial. Now, the photodiode has to be calibrated to determine the actual pulse energy for each shot. Using a power meter, the average power after the objective is measured at 100 kHz for multiple power levels set by the variable neutral density filter. The amplitude on the photodiode is then recorded for each measured average power.

2.4 Post-Trial Analysis

Following the ablation trial, an autocorrelation function is fit to the pulse width trace from before and after the trial and then deconvolved to produce the actual pulse intensity function. The RegA pulses take the form of a $sech^2$ function given by combining equations 1.4 and 1.5. The FWHM of the pulse can then be recorded.

The photodiode energy calibration is completed by using the average powers and repetition rates recorded at the end of the trial. The energy of each pulse can be determined using the relationship in equation 1.1. The beam profiles from the beam profiler and a calibration factor are utilized to find the area of the beam spot at focus. The pulse energies divided by the beam spot area yield their fluences.

Next, the sample is moved to an external optical microscope. Using the hand drawn sample map, the ablation craters for each delay are located and imaged. The crater images are analyzed using ImageJ software. The pixel scale for each image is calibrated by inputting a previously known distance. The craters are then highlighted, and their areas are recorded.

For area-delay trials, the ablation areas at each delay are averaged. The average areas are plotted in an area vs delay autocorrelation curve. An exponential function as shown in equation 1.8 is fit to the curve and the mean lifetimes are extracted for both positive and negative delay. For ablation threshold trials, the ablation areas and their respective pulse energies for each delay are averaged. Then, the pulse energies are converted to fluences. The ablation area averages are plotted against their respective fluence averages in a Liu plot and fit to a logarithmic or power function as given in equations 1.9 or 2.0. The x-intercept of the fit corresponds to the ablation threshold at each delay. Finally, the measured thresholds are plotted against their delays and a curve is fit to the data.

CHAPTER 3: RESULTS

3.1 MoS$_2$ – Ablation Area vs Delay

A trial was conducted on a MoS$_2$ film on sapphire substrate. The pulse fluence

was set to .3717 $\frac{nJ}{\mu m^2}$. The sample was ablated at 12 different delays for both positive and

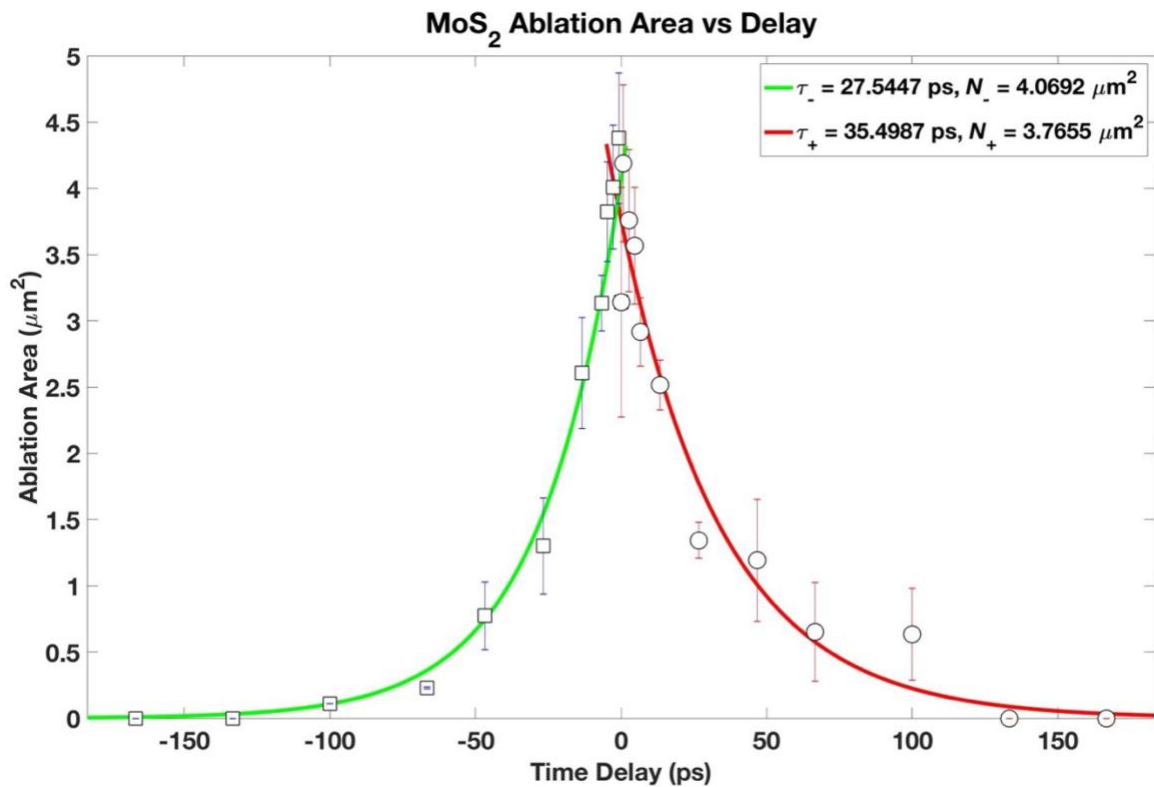negative delay. The resulting autocorrelation curve is presented in figure 3.1.

Figure 3.1: MoS$_2$ Ablation Area vs Delay

An exponential function of one term was fit to the negative and positive delay

data and presented in green and red respectively. The error bars for each data point

represent the sample standard deviation of the ablation areas measured at that delay. The

mean lifetimes τ_- and τ_+ as well as the coefficient amplitudes N$_-$ and N$_+$ were extracted.

The calculated amplitudes were within 7.8% of each other with an average of 3.917 μm^2.

The mean lifetimes had a percent difference of 25.2% with an average of 31.522 ps. The

two longest delays show no ablation occurred past ~±130 ps.

3.2 WS$_2$ – Ablation Area vs Delay

A trial was conducted on WS$_2$ flakes on sapphire substrate with the pulse fluence

set to .8463 $\frac{nJ}{\mu m^2}$. Ablation areas were measured at 17 different delays for both positive

and negative delay. The resulting autocorrelation curve is shown in figure 3.2.
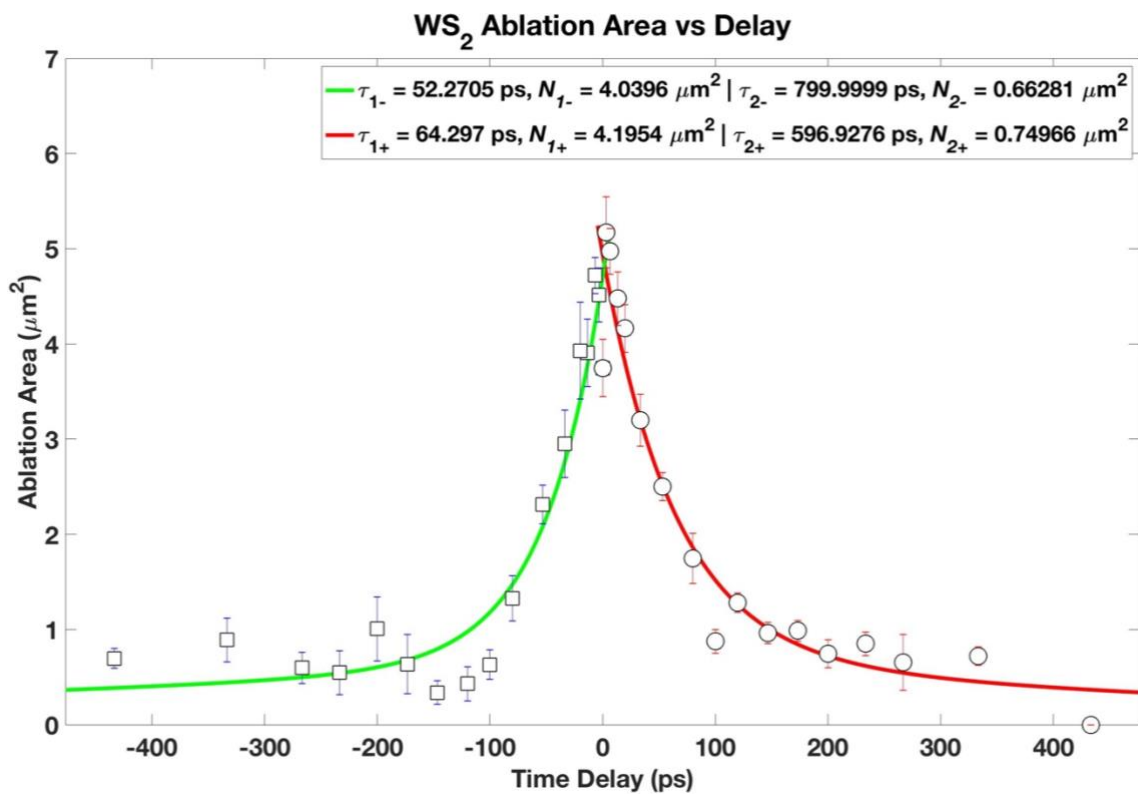
Figure 3.2: WS$_2$ Ablation Area vs Delay

Both the positive and negative delay data were fit with two-term exponential

functions. The delay regimes between -100 ps and 100 ps showed a significantly greater

rate of decay then of that in the tails. Moreover, the sub ±100 ps regimes showed similar

decay rates with mean lifetimes that were within 20.6% of each other with an average of

58.284 ps. The amplitude coefficients of this regime were very similar with a percent

difference of only 3.8% and an average of 4.118 μm^2. The decay rates in the tails yielded

a percent difference of 29.1% with an average of 698.464 ps. The corresponding

amplitudes were within 12.3% of each other with an average of .706 μm^2. Unlike -433

ps, no ablation occurred at +433 ps.

3.3 Graphene – Ablation Area vs Delay

A trial was conducted on graphene film on 90 nm Si/SiO2 substrate at a pulse

fluence of .6524 $\frac{nJ}{\mu m^2}$. The sample was ablated at 23 different negative delays and 24

different positive delays. The resulting autocorrelation curve is shown in figure 3.3.
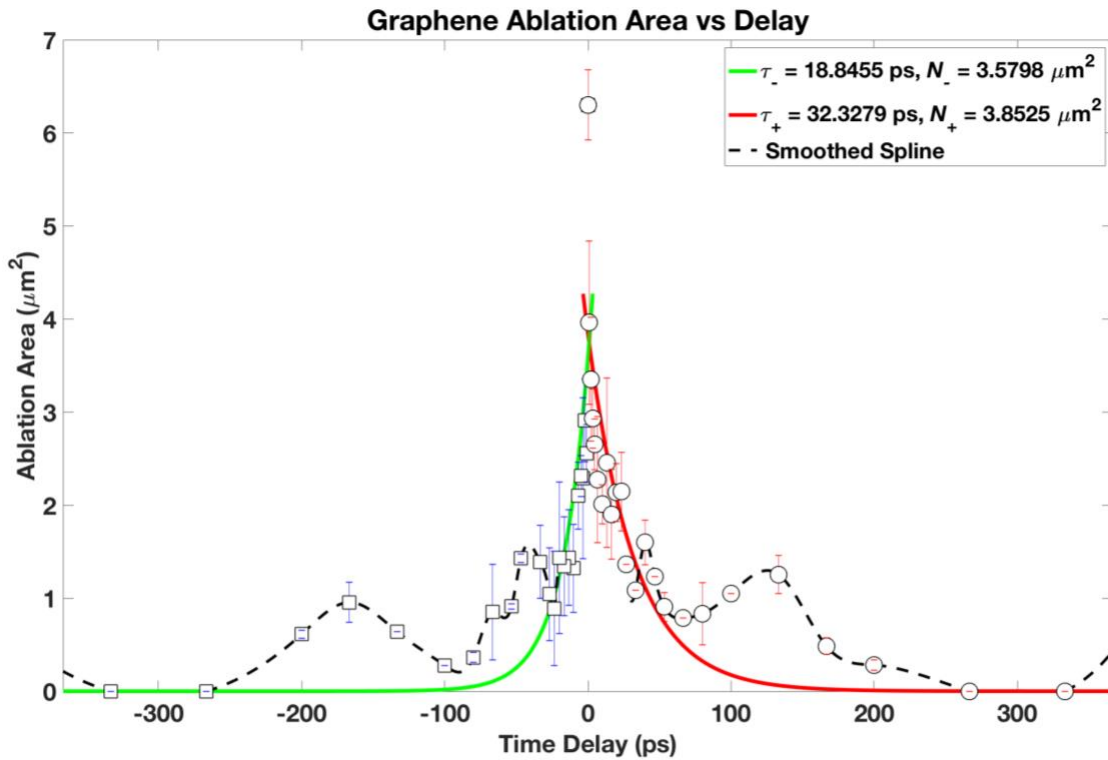

Figure 3.3: Graphene Ablation Area vs Delay

The graphene data showed high variation in ablation area for multiple delays.

Several pulses failed to produce an ablation crater. Those data points were excluded from

the averaging. At time-zero, the ablation area is 6.301 μm^2, making it significantly

higher than its neighboring delays. A smoothed spline function was fit to the data after

±30 ps and plotted with a dashed line. The two tails show symmetrical secondary peaks at

~ ±150 ps. Also, there are possible third peaks occurring at ±50 ps. A single-term

exponential fit yielded mean lifetimes that significantly differed by almost 52.7% at an

average of 25.587 ps. The amplitudes had a percent difference of 7.3% at an average of

3.716 μm^2. No ablation craters formed passed ~±250 ps.

<div align="center">3.4 MoS$_2$ – Ablation Threshold vs Delay</div>

An ablation threshold trial was conducted on a MoS$_2$ film on sapphire substrate.

Ablation craters were measured at 15 different delays. Figure 3.4 shows the Liu plots at

eight selected delays. The fitted curves were logarithmic in form as given in equation 1.9.

At most delays, the fits agree with the measured fluences, but the fit quality considerably

degrades at longer delays where ablation hole measurement became less precise. The

333.3 ps Liu plot is an example of where the fluence and area showed high standard

deviations and a poor fit. The fluences at threshold were plotted in terms of delay in

figure 3.5. Using residual analysis, it was determined that a linear fit agreed best with

points beyond 3.333 ps. The slope of the fit was found to be .4992 $\frac{J}{\mu m^2 \times s}$. Interestingly, at

time-zero there is a distinctively low threshold of ~.32 $\frac{nJ}{\mu m^2}$.
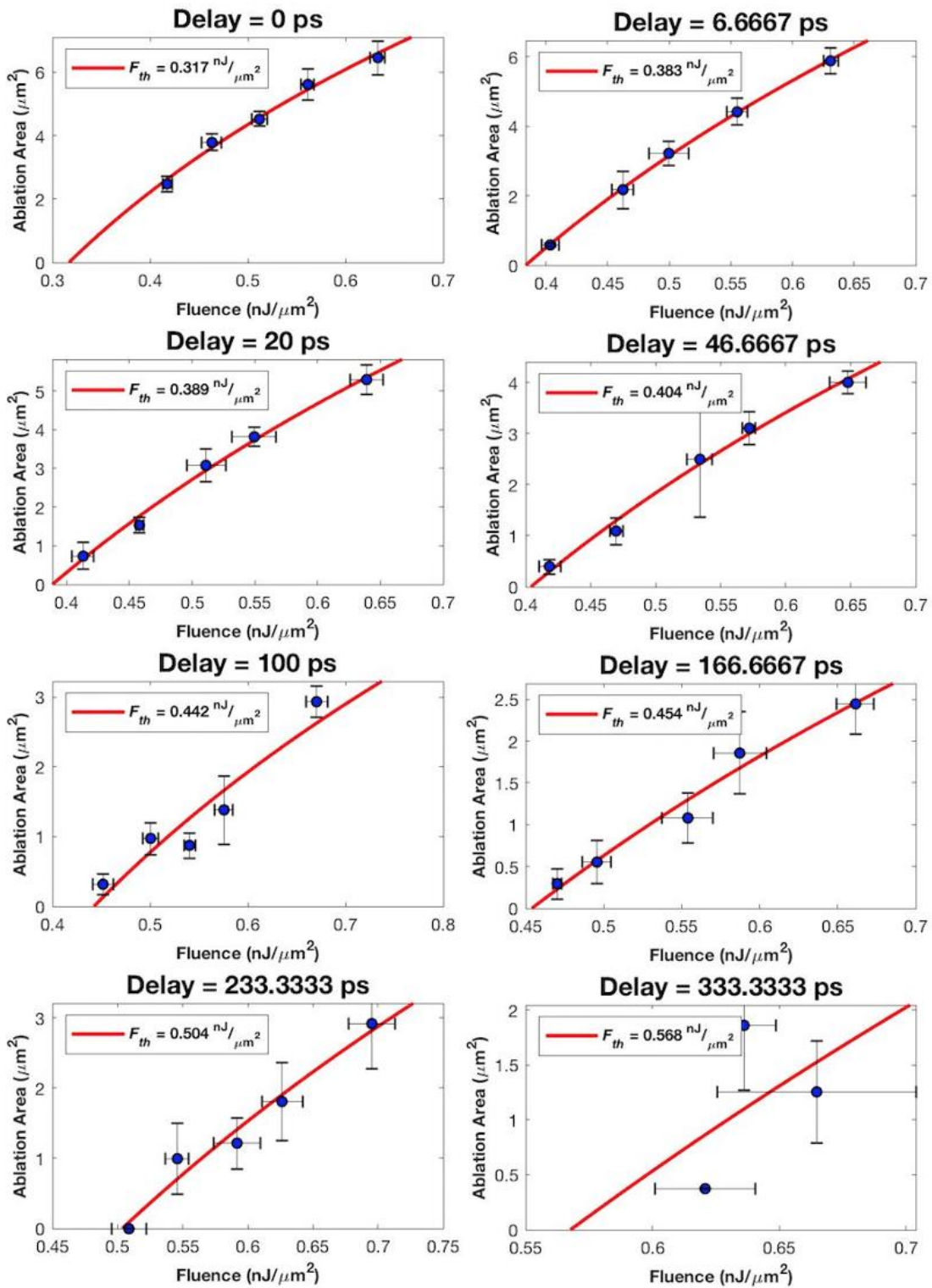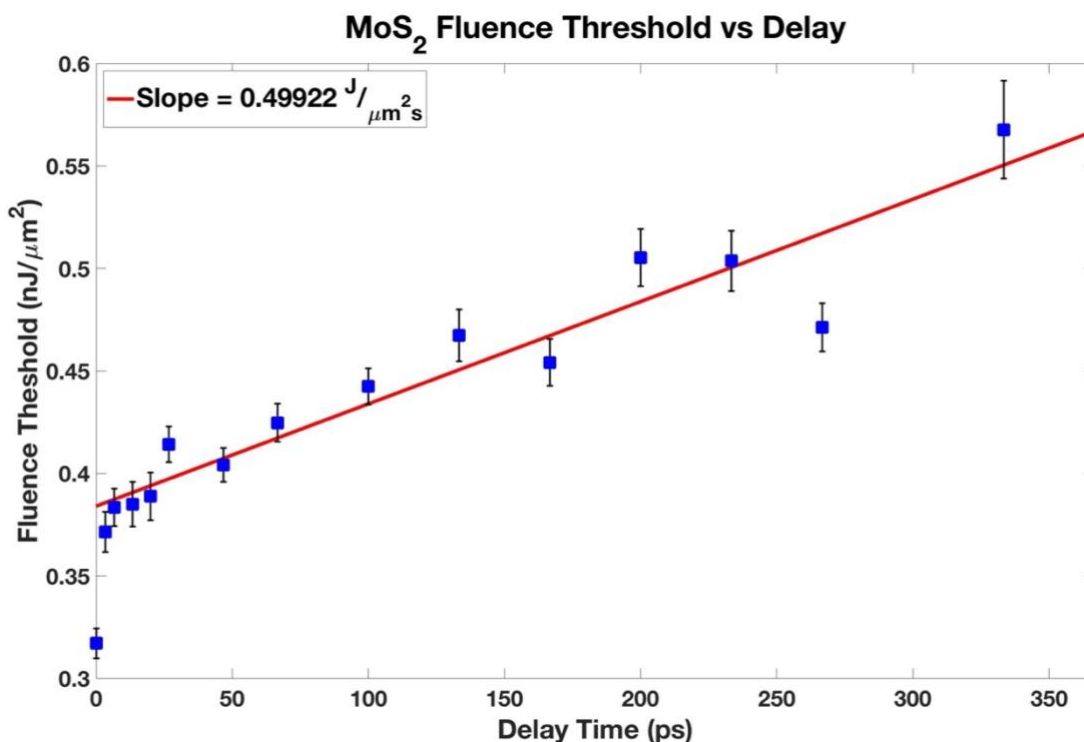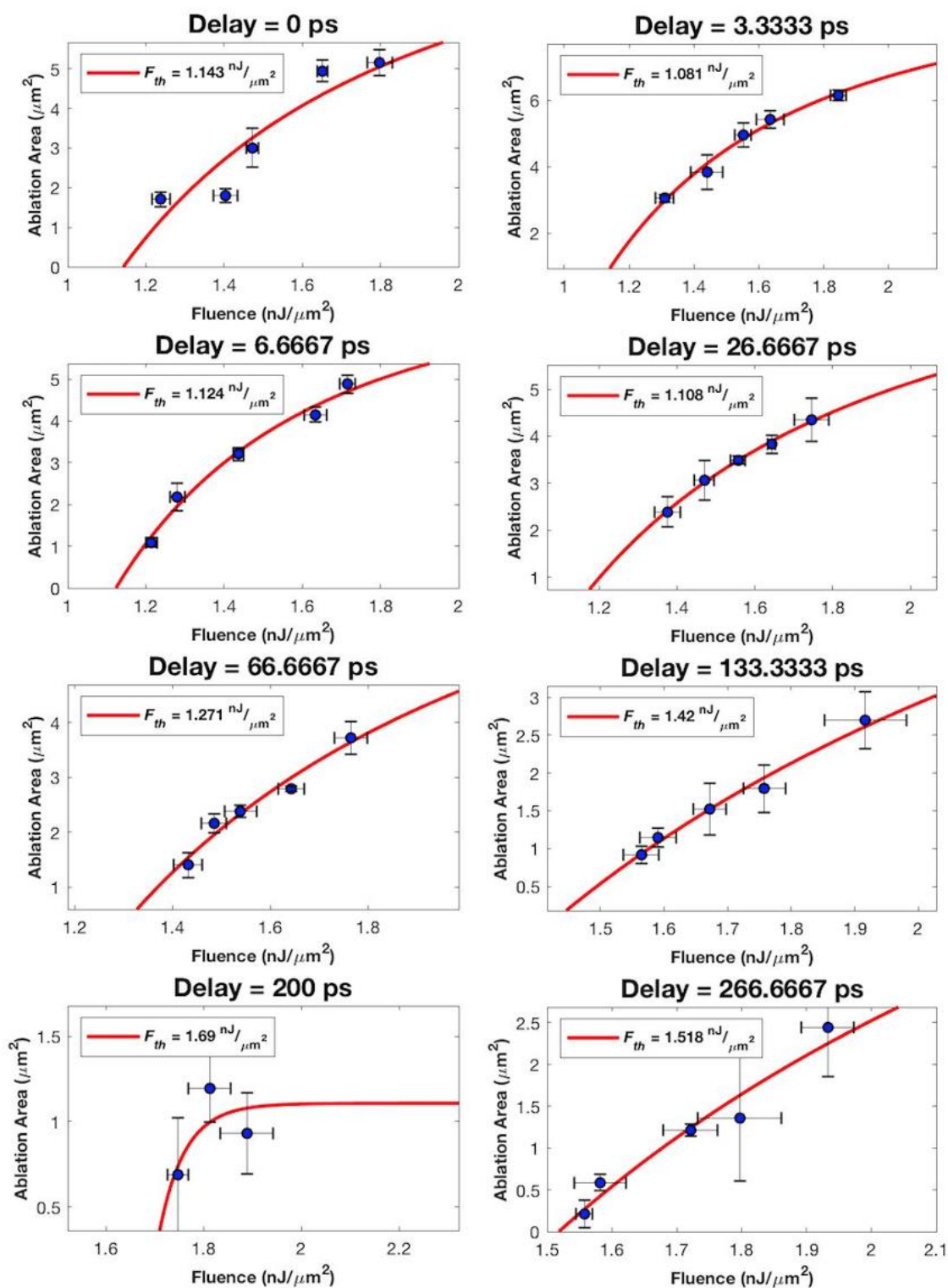
Figure 3.4: MoS$_2$ Liu Plots

Figure 3.5: MoS$_2$ Fluence Threshold vs Delay

3.5 WS$_2$ – Ablation Threshold vs Delay

An ablation threshold trial was conducted on a WS$_2$ flakes on sapphire substrate.

Data was taken for 20 different delays. Figure 3.6 shows the Liu plots at eight of the

delays. The fitted curves were power functions in the form of equation 1.9. At most

delays, the fits agree with the measured fluences, but as with MoS$_2$, the fit quality

worsens at longer delays where ablation hole measurement became less precise. The 200

ps Liu plot demonstrates a poor fit with only 3 data points. The fluences at threshold were

plotted in terms of delay in figure 3.7. The data was divided into two regimes with

distinct trends. A line of best fit was applied to each as shown by the red and green lines.

The rate of change for both is given by their slopes and was found to be 3.19 and .391

$\frac{J}{\mu m^2 \times s}$.

Figure 3.6: WS₂ Liu Plots
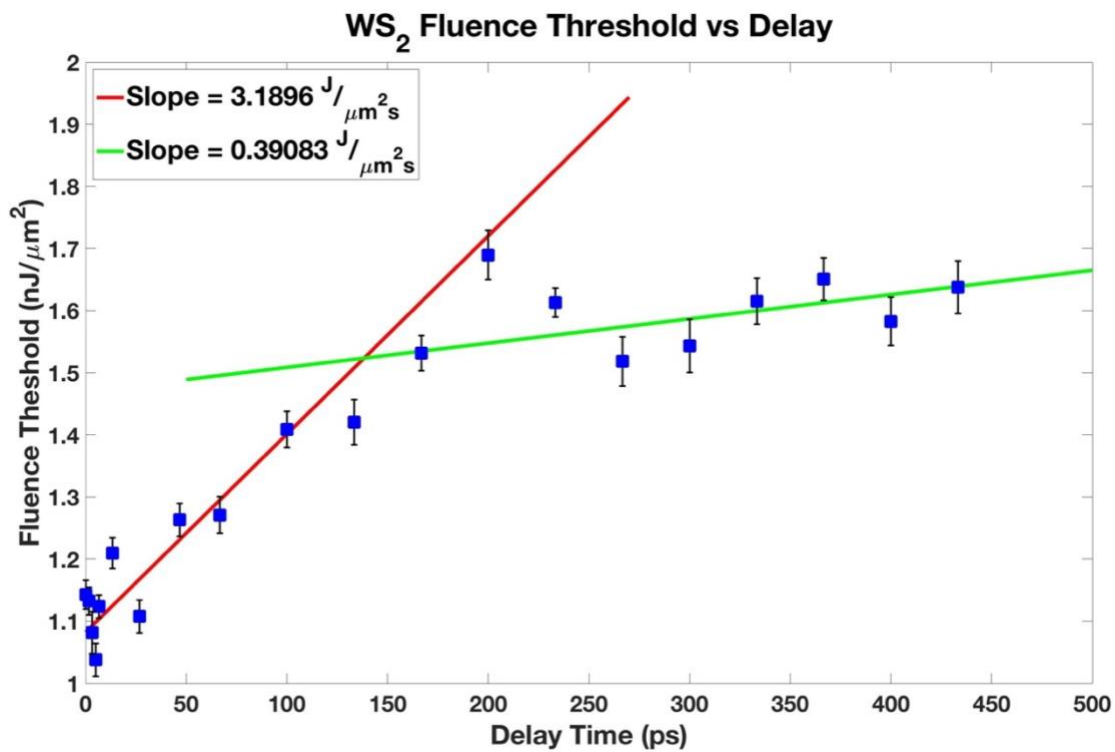
Figure 3.7: WS$_2$ Fluence Threshold vs Delay

CHAPTER 4: DISCUSSION AND CONCLUSIONS

Running trials below a two-shot threshold proved to be difficult. The required

pulse fluences yielded small ablation craters at the resolution limit of the sample

microscope. Craters on MoS_2 on Si/SiO_2 and WS_2 on sapphire were noticeable up through

~$\pm$300 ps delays with visibility diminishing at larger delays toward the tail ends.

However, graphene craters on 90 nm Si/SiO_2 were no longer visible past $\pm$75 ps and

could only be imaged using the external microscope during the post-trial analysis.

Ablation craters at large delays were as small as a .1 μm^2. At this size, the ImageJ

software only measured a couple dozen pixels within the ablation crater, causing rough

boundaries. Resultantly, the precision of the measured areas diminishes at large delays as

demonstrated in the data by the error bars.

Although multiple telescopes were added along the experimental set-up to

maintain beam collimation, diffraction of the beam was present. The distance between the

two ends of the translation stage was 130 mm. Therefore, a beam traveling on the

translational arm would propagate 13 cm farther with the mirror on the far end than when

the mirror is closest to the beam splitter. Any diffraction taking place could alter the size

of the beam at focus and produce inaccurate measurements of fluence and ablation area at

different delays.

Another source of error is the instability of the laser system. The Millennia pump

laser power output showed some fluctuations over the long duration of a trial. At times,

this would affect the measured amplitudes on the photodiode and produce lower or higher

pulse energies (<5%) than originally set. The RegA and Tsunami were both monitored

and tuned to compensate for these fluctuations over the long term, however, short term variation could not be prevented.

4.1 MoS$_2$

The MoS$_2$ film was continuous with a somewhat rough texture showing several small (<.1 μm) but consistent imperfections throughout the film. Many of these spots were regions of bilayer crystal formation or minor defects that occurred during the transfer to Si/SiO$_2$ substrate.

The mean lifetime of 31.5 ps determined from the exponential fits in figure 3.1 agrees with one mean lifetime of ~23 ps extracted for C-excitons in previous pump-probe experiments[11]. Within this time, contributions of charge populations generated by self-separation of C-excitons in momentum space could form hot carriers that enhance the ablation process[12].

The fluence thresholds maintained a relatively constant rate of change with increasing delay in figure 3.3. However, below 1 ps, the threshold drops significantly. The likely cause is at ~0 fs delay, a high density of excited charge carriers is in the conduction band. After ~500 fs, the carriers relax to the exciton. Additionally, bandgap renormalization occurs in the first ~300 fs. The dynamics during this time are presumably very unlike that of the higher ps regime.

4.2 WS$_2$

The WS$_2$ triangular flakes were transferred and had an average side length of ~120 μm. Each flake encompassed enough space for 5-6 delay shot groupings. Unlike the negative delay, the positive delay data shows ablation area going to 0 at 433 ps. This discrepancy is likely due to diffraction affecting the beam spot at such a large delay.

Moreover, the delay stage may not be long enough to accurately represent the entire tail lifetimes. The two mean lifetimes extracted from the fits could represent two different processes contributing to enhanced ablation. Pump-probe experiments have determined that after excitation into the conduction band, the A-exciton mostly reappears at 50 ps with full recovery occurring at 250 ps.[13] This is on par with the 58.3 ps lifetime of the first exponential term. The remaining ~700ps lifetime may correspond to some non-radiative decay process.

As with MoS_2, WS_2 likely endures similar femtosecond dynamics like bandgap renormalization near time-zero. Consequently, the fluence thresholds are notably low at some of the shortest delays in figure 3.7. The two distinctive rates of threshold change could be related to the two time regimes from figure 3.1. The data points from the first fit extend to 200 ps. This is still in agreement with the recovery lifetime of the exciton. Likewise, the slower varying regime (>200ps) may correspond to some non-radiative process.

4.3 Graphene

The continuous graphene film was grown as is and was never transferred. It showed a consistent web of cracks throughout the film. During ablation, these cracks were avoided. Ablation craters were often nonuniform due to graphene's tendency to fold back onto itself during femtosecond laser ablation[14]. The folds typically formed along one side of the crater. Ablating on or near a crack would almost always result in folding.

Graphene showed interesting behavior at time-zero. The ablated area is significantly greater than at any other delays. This behavior suggests that the ablation mechanism is likely coulomb explosion. Other autocorrelation experiments show that

with graphite[15], a material composed of several layers of graphene, coulomb explosion takes place in ~100 fs which explains why it is only present at approximately zero time delay. Two pulses with a width of ~180 fs approximately overlapped will interact with the graphene well below 100 fs. The intense pulses cause a cluster of carbon atoms to free their electrons resulting in high ionization. The ionized cluster experiences strong coulomb repulsion that eventually overcomes its cohesive energy. An explosion of ions with high kinetic energy ensues also disintegrating the neighboring clusters of carbon atoms and ultimately ablating a larger region.

The graphene data appears messy with high variation that is likely due to folding. Consequently, the fits for both positive and negative delays differed greatly. However, the symmetrical tail peaks defined by the spline curve are possibly the result of mechanical resonance in the graphene's structural rigidity. The two later peaks at ~±50 ps and ~±150 ps correspond to 20 GHz and 6.7 GHz frequencies respectively. The natural frequencies of mechanical resonances in graphene have been recorded in the low GHz range which may explain the enhanced ablation when at resonance.

CHAPTER 5: SUMMARY AND FUTURE WORK

In this experimental study, two-pulse autocorrelation was used to investigate the timescales of enhanced ablation in CVD grown monolayer MoS_2 and WS_2. For comparison, another common 2D semiconductor, graphene was also studied. The laser system produced 800 nm pulses with an average width of ~180 fs. The experimental set-up utilized an autocorrelator with a Michelson interferometer geometry to split a pulse into two with equal energy. A motorized stage along one arm delayed one pulse with respect to the other before they were focused with an objective onto the sample. The first incident pulse produced a reversible electronic response in the samples, leading to enhanced ablation with the arrival of the second pulse. The ablation crater areas were measured and analyzed as a function of delay. In addition, the pulse fluence threshold as a function of delay was examined.

The MoS_2 trials showed some evidence that its ~130 ps enhanced ablation process is correlated to a C-exciton lifetime of ~23 ps. The exponential fit to the ablation area yielded a similar mean lifetime of 31.5 ps for the enhanced ablation. Also, it was found that the fluence threshold demonstrated a linear rate of change with respect to delay. A steep fall off occurred near time-zero which is attributed to the relaxation of charge carriers from the conduction band to the exciton and band gap renormalization occurring below 1 ps.

The WS_2 trials presented strong evidence that the mean lifetime of enhanced ablation is associated with the A-exciton relaxation lifetime from the band gap. A two-term exponential fit yielded lifetimes of 58.3 ps and ~700 ps. The first of which matches the reemergence of the exciton after excitation at ~50 ps. The threshold-delay relationship

showed two distinct regimes of positive threshold variation before and after 200 ps. The first regime varies 8 times quicker than the second over a time that is still reasonably aligned with the exciton lifetime. Femtosecond delay also showed some threshold fall off from band gap renormalization dynamics.

The graphene data yielded poor exponential decay fits. The well documented folding mechanism in graphene also contributed to the cratering during ablation. After a ~250 ps delay, all enhanced ablation ceased. There is strong evidence for coulomb explosion at time-zero which has been similarly reported in graphite. Also, resonance peaks at ~150 ps are likely the result of mechanical resonances in graphene.

In future studies, ablation trials will be conducted on many of the other monolayer TMDs. It will be important to characterize the substrate dependence of enhanced ablation. Varying the material and thickness of the substrate will yield interesting results. Additionally, trials can be run over a two-shot fluence threshold to study how defect generation (relevant in multi-shot ablation) and enhancement together play a role in autocorrelated ablation.

REFERENCES

[1]J.M. Liu. *Optics Letters*. **7** (5), 196-198 (1982)

[2]S. Preuss, M. Späth, Y. Zhang, M. Stuke. *Applied Physics Letters*. **62**, 3049 (1993)

[3]Q.H. Wang, et al. *Nature Nanotechnology*. **7**, 699-712 (2012)

[4]A. Chernikov, et al. *Physical Review Letters*. **113**, 076802 (2014)

[5]M. Chhowalla, et al. *Nature Chemistry*. **5**, 263-275 (2013)

[6]B. Radisavljevic, et al. *Nature Nanotechnology*. **6**, 147-150 (2011)

[7]S. Bertolazzi, J. Brivio, A. Kis. *ACS Nano*. **5** (12), 9703-9709 (2011)

[8]H. Liu, Y. Li, Y. You, et al. *Nature Phys*. **13**, 262–265 (2017)

[9]K.S. Novoselov, et al. *Proceedings of the National Academy of Sciences*. **102** (3), 10451-10453 (2005)

[10]Y.H. Lee, et al. *Advanced Materials*. **24** (17), 2320-2325 (2012)

[11]L. L. Wang, et al. *Nature Communications*. **8**, 13906 (2017)

[12]D.Kozawa, et al. *Nature Communications*. **5**, 4543 (2014)

[13]A. Chernikov, et al. *Nature Photonics*. **9**, 466–470 (2015)

[14]J. Yoo, et al. *Appl. Phys. Lett.* **100**, 233124 (2012)

[15]A. Kaplan, et al. *Applied Physics A*. **92** (4), 999 (2008)